Check for updates

Wiley
International Journal of Energy Research
Volume 2025, Article ID 3924822, 10 pages
https://doi.org/10.1155/er/3924822

WILEY

Research Article

Interfacial Charge Dynamics and Optical Constraints in Chlorophyll-Functionalized TiO_2 Nanotube Arrays

Abraham Seo,[1] **Kanghyun Lee**,[1] **Yujin Lee**,[1] **Seyeon Kim**,[1] **Sanghyuk Lee**,[2] **Suyeon Chae**,[1] **Inho Nam**,[3] **Sungju Yu**,[2] **and Soomin Park**[1]

[1]*School of Energy, Materials and Chemical Engineering, Korea University of Technology and Education, Cheonan 31253, Republic of Korea*
[2]*Department of Energy Systems Research and Department of Chemistry, Ajou University, Suwon 16499, Republic of Korea*
[3]*Department of Chemical Engineering, Department of Advanced Materials Engineering, Department of Intelligent Energy and Industry, Chung–Ang University, Seoul 06974, Republic of Korea*

Correspondence should be addressed to Inho Nam; inhonam@cau.ac.kr, Sungju Yu; sungjuyu@ajou.ac.kr, and Soomin Park; smpark@koreatech.ac.kr

Received 10 July 2025; Revised 9 October 2025; Accepted 29 October 2025

Academic Editor: Weixin Guan

Copyright © 2025 Abraham Seo et al. International Journal of Energy Research published by John Wiley & Sons Ltd. This is an open access article under the terms of the Creative Commons Attribution License, which permits use, distribution and reproduction in any medium, provided the original work is properly cited.

Natural pigments offer promise for visible-light harvesting, but their exciton transport and photostability remain limiting factors. Here, we present a biohybrid photoelectrode comprising chlorophyll (Chl) immobilized onto anodized TiO_2 nanotube (TNT) arrays. Controlled deposition yields a hierarchical trilayer structure featuring capillary-driven infiltration and tunable optical thickness. Transient photocurrent measurements reveal a synergistic regime in which moderate Chl loading and optimal illumination maximize charge generation. Spectral and time-resolved analyses indicate that exciton quenching occurs via energy delocalization and interfacial electron injection. In contrast, excessive loading leads to exciton confinement, self-shading, and trap-assisted recombination, which collectively suppress charge extraction. These results delineate a design window in which light absorption, exciton mobility, and photostability are cooptimized, offering practical guidance for integrating natural pigments into photoelectrochemical (PEC) systems.

Keywords: biohybrid photoelectrodes; chlorophyll; exciton transport; interfacial electron injection; TiO_2 nanotube arrays

1. Introduction

The accelerating need for sustainable energy conversion continues to motivate photoelectrochemical (PEC) strategies that harvest sunlight in aqueous environments. Despite steady advances, efficient use of the visible region remains challenging [1, 2], largely because widely used wide-bandgap oxides exhibit weak absorption at wavelengths longer than 420 nm and often suffer from suboptimal charge separation and interfacial transfer [3, 4].

Natural photosynthesis provides principles for addressing these constraints. Photosynthetic antenna complexes organize pigments with nanometer precision to funnel excitation energy toward reaction centers with minimal loss [5, 6]. Chlorophyll (Chl) plays a central role through its conjugated macrocycle, which gives rise to strong absorption in the blue (Soret) and red (Q_y) bands and supports excitonic transport at ambient conditions [5, 7]. Translating this capability into synthetic PEC platforms requires not only spectral extension into the visible range but also control of exciton migration and timely electron injection at solid–liquid interfaces.

Chl and Chl-derived sensitizers have been combined with TiO_2 in dye-sensitized and PEC formats [8–10]. Many of these studies employed nanoparticulated films or molecular anchoring on flat substrates. Although they demonstrated visible-light response, several bottlenecks persist: aggregation-induced

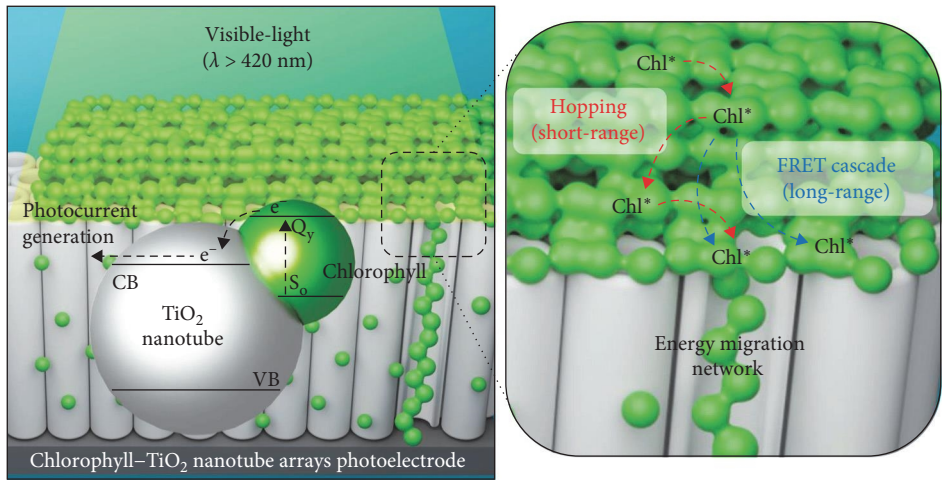


FIGURE 1: Schematic illustration of a Chl-TNT photoelectrode under visible-light irradiation ($\lambda > 420$ nm), depicting light absorption by Chl, exciton migration through a short-range hopping and long-range Förster-type cascade network, and subsequent electron injection into the conduction band of TiO_2 for photocurrent generation.

quenching that shortens exciton diffusion lengths [11], limited electrical percolation in disordered films, photochemical instability under high photon flux, and uncertain electronic coupling between Chl aggregates and the oxide in the absence of specific anchoring chemistries [6, 12]. As a result, it remains difficult to separate spectral benefits from transport and stability limitations, and mechanistic descriptors that connect pigment loading, optical flux, and charge-transfer dynamics are still underdeveloped.

Here, we interface Chl with vertically aligned TiO_2 nanotube (TNT) arrays to establish a mechanistic framework for visible-light-responsive biohybrid photoelectrodes (Figure 1). The TNT architecture provides straight electron pathways, a large internal surface area, and tunable geometric parameters that impact light management and electrolyte access [13, 14]. The open tubular morphology promotes capillary infiltration of Chl from acetone dispersions and constrains aggregation within nanoconfined domains, improving electronic communication with the oxide and reducing recombination relative to disordered films. This study examines whether Chl confined in ordered TNT arrays produces a controllable visible-light PEC response when exciton harvesting and interfacial electron injection are balanced. To that end, we (i) constructed a quantitative two-dimensional map that relates areal loading and incident visible-light flux to photocurrent, revealing a well-defined operating window; (ii) link device behavior to photophysical kinetics by time-resolved photoluminescence (TRPL) on the same architecture, evidencing rapid quenching consistent with efficient electron injection; (iii) identify the high-flux performance limit using reactive-oxygen-species (ROS) controls, showing that photocurrent roll-off originates primarily from ROS-driven degradation. The fabrication route is simple and scalable—anodization, brief ultrasonic cleaning, annealing to anatase, and controlled drop-casting—without metal complexes, covalent linkers, or vacuum processing.

These results provide a clear rationale for pairing Chl with TNT arrays: strong visible absorption and mobile excitations from Chl, favorable energetics and chemical robustness from TiO_2, and nanoconfinement that enhances interfacial contact while shortening transport distances. Relative to prior Chl-TiO_2 studies that largely focused on dye-sensitized or nanoparticulate films, this work delivers, to our knowledge, the first quantitative loading-flux design map correlated with excitonic kinetics on an ordered PEC architecture, together with direct evidence of negligible pigment dissolution in aqueous electrolyte. The framework converts empirical tuning into transferable design rules for natural or synthetic chromophores on oxide scaffolds and delineates practical levers—loading, photon flux, and tube geometry—for engineering durable, visible-light-active PEC electrodes.

2. Experimental Section

2.1. Fabrication of TNT Array. TNT arrays were prepared by anodizing titanium foils (99.7%, trace metals basis, Sigma–Aldrich; 5.0 cm × 1.0 cm, 0.127 mm thick). Prior to anodization, the foils were ultrasonically cleaned for 10 min each in acetone, ethanol, and deionized (DI) water. Anodization was performed at 30 V for 1 h at 25°C in an ethylene glycol electrolyte containing 0.3 wt.% NH_4F (97%, Junsei) and 5 vol.% DI water [15]. A DC power supply (TOYOTECH) was used, with the Ti foil as the anode and a platinum plate as the counter electrode, positioned 3.5 cm apart (Supporting Information: Figure S1). Immediately after anodization, the films were rinsed thoroughly with ethanol and DI water, followed by an additional ultrasonication step (30 min, ethanol bath) to remove superficial nanograss and debris and to expose unobstructed tube apertures across the film. The electrodes were then dried in air at approximately 25°C overnight. Finally, the TNT arrays were annealed in air at 450°C for 2 h to convert the oxide to the anatase phase and to remove residual fluoride species.

2.2. Extraction of Chl. Chl was extracted from fresh spinach leaves obtained from a local market and used within 24 h. To prevent thermal- and photoinduced degradation, all steps were carried out in a 4°C cold room under low light; tubes were foil-wrapped or amber. Leaves were rinsed and blotted

ijer, 2025, 1, Downloaded from https://onlinelibrary.wiley.com/doi/10.1155/er/3924822 by Chung-Ang University, Seoul, Wiley Online Library on [30/11/2025]. See the Terms and Conditions (https://onlinelibrary.wiley.com/terms-and-conditions) on Wiley Online Library for rules of use; OA articles are governed by the applicable Creative Commons License

dry, and homogenized in phosphate-buffered saline (PBS, pH 7.4, Sigma–Aldrich). The homogenate (≈30 mL) was centrifuged at 12,000 rpm for 15 min at 4°C, and the supernatant was discarded. Each pellet was resuspended in 20 mL of acetone (analytical grade, ≥99.8%, Daejung) to solubilize Chl and centrifuged again under the same conditions. The resulting supernatant (Chl-acetone extract) was collected and stored at 4°C in the dark until use [16]. For spectroscopic quantification of Chl a and Chl b, the crude extract was diluted 40-fold with acetone, transferred to a 1 cm quartz cuvette, and measured in absorbance mode on a UV–vis spectrophotometer (V-770, JASCO). Chl a and Chl b concentrations were determined using the following simultaneous equations:

$$\text{Chl a} = 13.71 \times (\text{OD}_{646.6} - \text{OD}_{750}) - 2.85 \times (\text{OD}_{663.6} - \text{OD}_{750}),$$

$$\text{Chl b} = 22.39 \times (\text{OD}_{646.6} - \text{OD}_{750}) - 5.42 \times (\text{OD}_{663.6} - \text{OD}_{750}),$$

$$\text{Total Chl} = \text{Chl a} + \text{Chl b}.$$

The numerical coefficients (13.71, 22.39, 2.85, and 5.42) were originally derived by Porra et al. [17] from extinction coefficients of purified Chl a and b. These resolve the spectral overlap between the two pigments. Optical densities (ODs) were measured at 646.6, 663.6, and 750 nm, with the 750 nm baseline serving as a correction for turbidity and background scattering using an acetone blank (see details in Supporting Information: Note S1).

2.3. Preparation of Chl-Coated TNT Arrays Photoelectrode. Chl, extracted as described above, was deposited onto the surface of TNT array electrodes via a drop–casting method. To ensure consistency, the Chl content-calculated using the previously described spectroscopy method, was normalized to the geometric surface area of each TNT array electrode, yielding a controlled loading value in units of $\mu g\,cm^{-2}$ (Supporting Information: Table S1). For each sample, a precise volume of Chl-acetone solution was dispensed onto the TNT arrays' surface, ensuring complete coverage while avoiding localized accumulation or inhomogeneous distribution. After casting, the electrodes were dried overnight in the dark at 4°C to preserve the structural integrity of the Chl layer and prevent photodegradation [18]. The resulting Chl-TNT arrays photoelectrodes were used within 48 h of preparation to minimize the effects of pigment degradation overtime.

2.4. Characterizations. The surface morphology of the Chl-TNT arrays electrodes was examined using field-emission scanning electron microscopy (FE-SEM, Apreo S HiVac, FEI Company) operated at 15 kV. Cross-sectional imaging was enabled via focused ion beam (FIB) milling (XFlash 6i30, Bruker), and elemental mapping was conducted using an energy-dispersive X-ray spectrometer (EDS, XFlash 6i100, Bruker). Crystalline phase identification was carried out using X-ray diffraction (XRD, D8 ADVANCE, Bruker) with Cu Kα radiation at 40 kV and 30 mA. Diffraction patterns were collected over a 2θ range of 10°–80°. Surface chemical states were analyzed by X-ray photoelectron spectroscopy (XPS, K–Alpha+, Thermo Fisher Scientific). The binding energies of Ti 2p and O 1s were calibrated using the C 1s peak at 284.6 eV as the reference. The crystalline phase state and defect-related disorder of the TNT arrays were examined by Raman spectroscopy (LabRam Soleil, HORIBA Scientific). Spectra were collected in the range of 100–800 cm^{-1}. Optical absorption characteristics were measured using UV–visible diffuse reflectance spectroscopy (UV–DRS, V-770, JASCO) equipped with a 60 mm integrating sphere. Spectra were collected using diffuse reflectance methodology to evaluate the optical properties of pristine and Chl-coated TNT array electrodes. Raw reflectance R(λ) was converted to pseudo-absorbance $\widetilde{A}(\lambda) = \log(1/R)$ for qualitative analysis. TRPL measurements were performed using a spectrofluorometer system (FS5, Edinburgh Instruments) equipped with a time-correlated single-photon counting (TCSPC) module. The samples were excited using a 405 nm picosecond pulsed diode laser (EPL-405, Edinburgh Instruments). The emission signal was collected at 660 nm using a photomultiplier tube (PMT) detector under right-angle geometry. The instrument response function (IRF) was recorded under identical TCSPC conditions using appropriate nonemissive references, yielding an FWHM of 0.54–0.69 ns. Electrochemical impedance spectroscopy (EIS) measurements were carried out at open circuit potential using a 10 mV AC perturbation over the frequency range of 100 mHz–100 kHz, with a logarithmic sweep of 10 points per decade.

2.5. PEC Measurements. PEC measurements were performed using a potentiostat (VSP-400, BioLogic) in a standard three-electrode configuration (Supporting Information: Figure S1). The Chl-TNT arrays on Ti served as the working electrode (coated region immersed; uncoated top edge left above the electrolyte for electrical connection), an Ag/AgCl (1 M KCl) electrode was used as the reference, and a Pt plate as the counter electrode. The working and counter electrodes were aligned parallel to the light path and separated by 3.5 cm. Electrical contact to the potentiostat was made with alligator clips attached to the unimmersed top edges of Ti and Pt; the reference electrode was inserted independently between them. The electrolyte was a 100 mM Na_2SO_4 aqueous solution. Illumination was provided by a 300 W Xenon lamp (6258, Newport), equipped with an AM 1.5G filter and a long-pass filter ($\lambda > 420$ nm). The irradiation at the electrode surface was measured using an optical power meter (843-R, Newport) with a 0.93 cm diameter detector. For wavelength-dependent measurements, monochromatic light was selected using band-pass filters. Unless otherwise noted, photocurrent was recorded at an applied bias of +0.48 V vs. Ag/AgCl [19].

3. Results and Discussion

Chl was extracted from spinach leaves, and TNT arrays were prepared by anodizing Ti foils. The resulting TNT arrays

ijer, 2025, 1, Downloaded from https://onlinelibrary.wiley.com/doi/10.1155/er/3924822 by Chung-Ang University, Seoul, Wiley Online Library on [30/11/2025]. See the Terms and Conditions (https://onlinelibrary.wiley.com/terms-and-conditions) on Wiley Online Library for rules of use; OA articles are governed by the applicable Creative Commons License

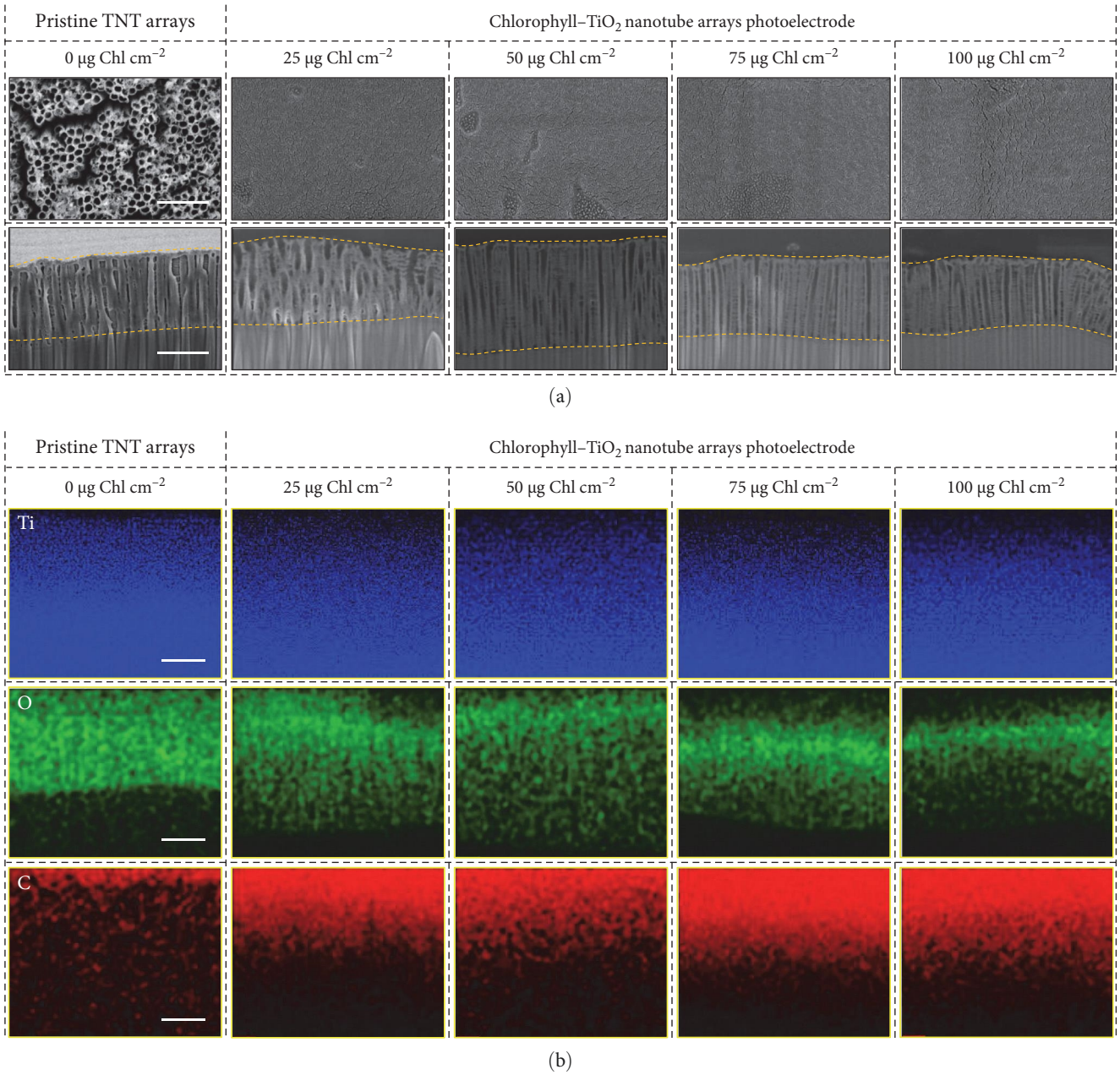


FIGURE 2: (a) Top-view and cross-sectional SEM images of TiO_2 nanotube array photoelectrodes with varying Chl loading amounts. (b) Corresponding EDS elemental maps of Ti (blue), O (green), and C (red). Scale bars: 500 nm.

exhibited well-opened tube apertures with uniform morphology (Supporting Information: Figure S2). The hierarchical Chl-TNT structures were fabricated via a drop-casting process, enabling direct immobilization of Chl onto the nanotube surface. As shown in Figure 2a, the deposited Chl formed a uniform coating across the TNT arrays at all loading levels, with no apparent aggregation or surface roughening.

Cross-sectional SEM revealed a well-defined trilayer architecture composed of a surface Chl layer, an underlying TNT layer (≈850 μm in height), and the Ti substrate. Elemental mapping (Figure 2b) confirmed this configuration, showing a strong carbon signal, attributed to Chl, both on the surface and within the nanotube channels, consistent with capillary-driven infiltration. Of note, the diameter of the nanotube channels was selected as 45–60 nm, which lies within the optimal range for PEC activity (Supporting Information: Figure S3). The deposited Chl concentration was controlled in the range of 156–223 mg cm^{-3} (Supporting Information: Table S1). The Chl overlayer thickness increased linearly with areal loading, reaching up to 5.2 μm at the highest deposition condition (Supporting Information: Figure S4), as determined from high-resolution cross-sectional SEM analysis.

Raman spectroscopy of the anodized TNT arrays confirmed the formation of phase-pure anatase, displaying sharp

ijer, 2025, 1, Downloaded from https://onlinelibrary.wiley.com/doi/10.1155/er/3924822 by Chung-Ang University, Seoul, Wiley Online Library on [30/11/2025]. See the Terms and Conditions (https://onlinelibrary.wiley.com/terms-and-conditions) on Wiley Online Library for rules of use; OA articles are governed by the applicable Creative Commons License

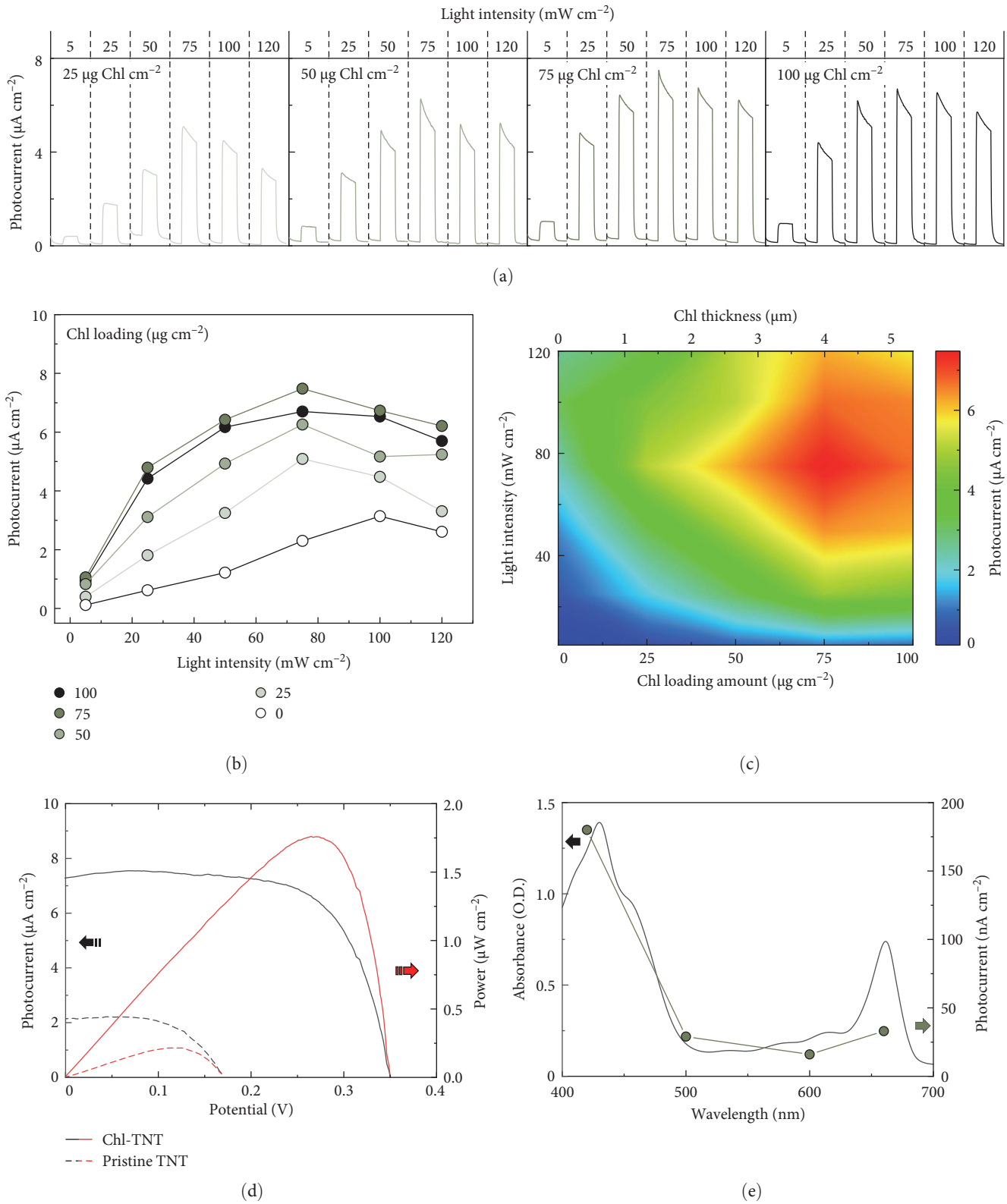


FIGURE 3: Continued.

ijer, 2025, 1, Downloaded from https://onlinelibrary.wiley.com/doi/10.1155/er/3924822 by Chung-Ang University, Seoul, Wiley Online Library on [30/11/2025]. See the Terms and Conditions (https://onlinelibrary.wiley.com/terms-and-conditions) on Wiley Online Library for rules of use; OA articles are governed by the applicable Creative Commons License

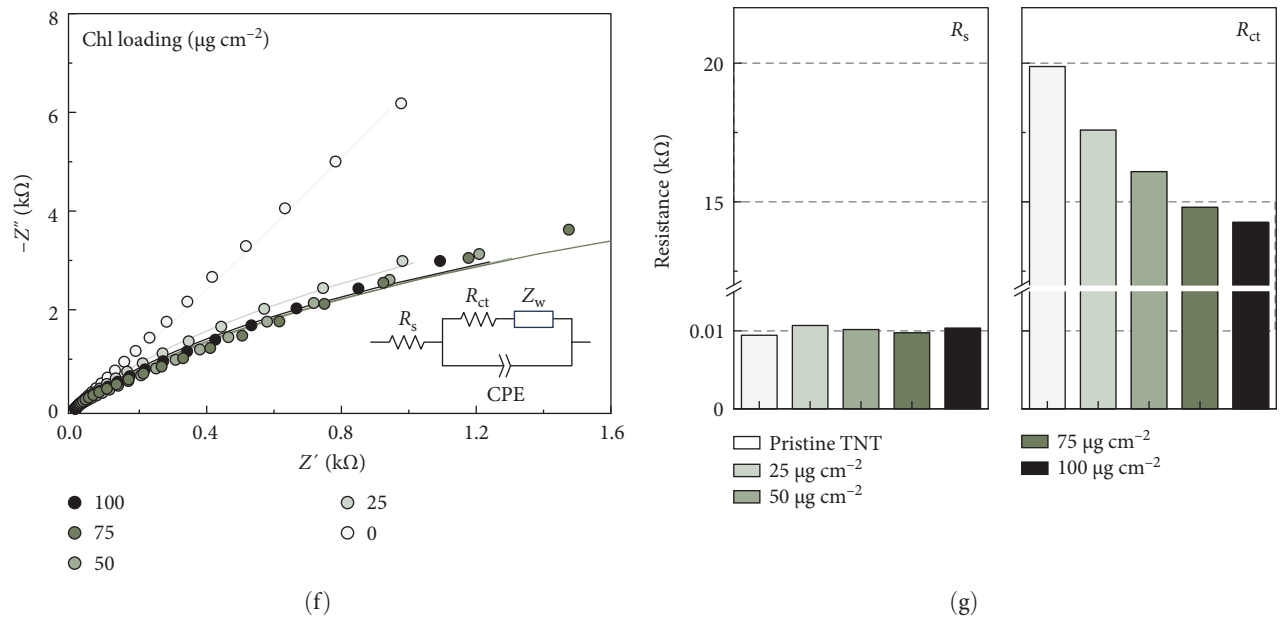


FIGURE 3: (a) Photocurrent responses of Chl-TNT photoelectrodes with varying Chl loading amounts under chopped visible-light irradiation ($\lambda > 420$ nm) at different light intensities. (b) Peak photocurrent values plotted as a function of both Chl loading and light intensity. (c) Contour plot mapping the photocurrent output as a function of areal Chl loading (indicative of layer thickness) and illumination intensity. (d) *I–V* characteristics of pristine TNT and Chl-TNT (75 μg cm^{-2} Chl loading) PEC cells under visible-light irradiation ($\lambda > 420$ nm, 75 mW cm^{-2}). (e) UV–vis absorption spectrum of Chl in solution compared with the corresponding photocurrent action spectrum of Chl-TNT electrodes, measured using band-pass filters. (f) Nyquist plots of Chl-TNT electrodes under illumination, together with equivalent circuit fitting (inset: circuit model used for fitting). (g) Extracted R_s and R_{ct} values from the equivalent circuit analysis as a function of Chl loading.

characteristic modes with no noticeable signs of disorder (Supporting Information: Figure S5). Consistent with this, XRD analysis (Supporting Information: Figure S6) confirmed that the characteristic diffraction peaks of TNT are well preserved after Chl loading, indicating that the anatase phase of TiO_2 remains the dominant crystalline structure. A broad feature near 20°, observed exclusively in the Chl-TNT array, is attributed to amorphous or semicrystalline organic aggregates, consistent with the spectral characteristics of disordered pigment films reported in earlier works [20].

XPS further confirmed chemical interactions at the Chl-TNT array interface. Upon Chl functionalization, the O 1s component associated with oxygen species near vacancy sites shifted from 530.3 to 531.2 eV (Supporting Information: Figure S7), while the lattice oxygen peak at 529.5 eV and the Ti 2p signals were unchanged. This selective shift indicates preferential interaction of Chl with surface oxygen vacancies on the TiO_2, providing molecular anchoring and enhancing interfacial electronic coupling [13, 21]. Consistent with such vacancy-mediated binding, fluorescence-based leaching measurements detected only a negligible fraction (<0.05%) of the initially loaded Chl after 15 h immersion (Supporting Information: Figure S8), confirming structural stability of the films under the conditions used for PEC measurements.

The PEC response of Chl-TNT photoelectrodes was evaluated under chopped visible-light ($\lambda > 420$ nm) at an applied bias of +0.48 V vs. Ag/AgCl, a potential relevant to water redox processes [19]. All samples produced prompt, reproducible on–off transients (Figure 3a), evidencing efficient photoinduced charge separation and extraction. Relative to unsensitized TNT arrays, Chl-functionalization increased the steady-state photocurrent by approximately fourfold (Figure 3b; Supporting Information: Table S2). The photocurrent rose with both Chl loading and irradiance and reached a maximum of 7.48 μA cm^{-2} at 75 μg cm^{-2} loading and 75 mW cm^{-2} illumination. At higher illumination levels; however, the photocurrent response saturated or decreased slightly, suggesting the onset of inner-filter effects and nonradiative losses under intense excitation. This nonlinearity was reproducible across the series with different Chl coverages. The corresponding contour plot (Figure 3c) identifies a synergistic regime in which moderate Chl loading, combined with optimal light intensity, produces the highest photocurrent output. These results highlight the importance of simultaneously tuning optical absorption and interfacial charge transport to maximize PEC efficiency in Chl-TNT architectures.

The current–voltage (*I–V*) characteristics of the Chl-TNT (75 μg cm^{-2} Chl loading) and pristine TNT PEC cells were measured under visible-light irradiation ($\lambda > 420$ nm, 75 mW cm^{-2}) (Figure 3d). The measurements were performed via linear sweep voltammetry, scanning from the open-circuit voltage (V_{oc}) to 0 V vs. Ag/AgCl. The Chl-TNT electrode exhibited a short-circuit current density (J_{sc}) of 7.5 μA cm^{-2} and a maximum output power density of 1.76 μW cm^{-2}, compared to 2.18 μA cm^{-2} and 0.21 μW cm^{-2}, respectively, for pristine TNT. The V_{oc} values were 350 mV for Chl-TNT and 170 mV for TNT, indicating that the incorporation of Chl extends the photovoltage generation into the visible range

ijer, 2025, 1, Downloaded from https://onlinelibrary.wiley.com/doi/10.1155/er/3924822 by Chung-Ang University, Seoul, Wiley Online Library on [30/11/2025]. See the Terms and Conditions (https://onlinelibrary.wiley.com/terms-and-conditions) on Wiley Online Library for rules of use; OA articles are governed by the applicable Creative Commons License

via efficient electron injection from photoexcited Chl (Chl*) into the TiO_2 conduction band. The elevated J_{sc} arises from both the additional visible-light photocurrent component and the maintenance of effective charge collection pathways within the TNT scaffold. Consequently, the maximum power output of the Chl-TNT electrode is 8.4-fold greater than that of the pristine TNT, demonstrating the synergistic contribution of enhanced photovoltage and photocurrent. The *I–V* curve for the same Chl-TNT electrode under full-spectrum simulated sunlight (AM 1.5G, 75 mW cm^{-2}) is shown in Supporting Information: Figure S9.

To identify the origin of the photocurrent, action spectrum measurements were conducted under monochromatic illumination. The resulting spectral response (Figure 3e) exhibited two prominent peaks centered at 420 and 660 nm, corresponding to the Soret and Q_y absorption bands of Chl, respectively, as verified by its UV–vis absorption profile [22–24]. This spectral match confirms that the photocurrent is driven by direct photoexcitation of Chl molecules. The action spectrum also correlates well with the electrode absorption profile obtained from diffuse-reflectance measurements (Supporting Information: Figure S10), further verifying that the observed photocurrent originates from immobilized Chl on the TNT substrate. Following excitation, electrons in the Chl unoccupied molecular orbital (LUMO, −1.27 V vs. NHE) undergo energetically favorable transfer to the conduction band (CB) of TiO_2 (−0.5 V vs. NHE) [25], thereby facilitating interfacial charge injection. This process establishes Chl as an effective photosensitizer, enabling visible-light activation of wide-bandgap TiO_2 through natural pigment integration.

To further elucidate the interfacial charge–transfer process, EIS was carried out under illumination for electrodes with varying Chl loadings (Figure 3f,g). The resulting Nyquist plots were fitted with an equivalent circuit consisting of R_s (series resistance), R_{ct} (charge transfer resistance), CPE (constant phase element), and Z_w (Warburg element). The fitted parameters revealed that R_s remained nearly constant at ~ 10 Ω for all electrodes, showing identical nonfaradaic contributions. However, R_{ct} decreased systematically with increasing Chl loading. This trend confirms that a thicker Chl layer facilitates interfacial electron injection into TiO_2.

Notably, while photocurrent reached a maximum at 75 μg cm^{-2} and slightly declined at 100 μg cm^{-2}, R_{ct} continued to decrease, indicating that interfacial charge transfer remained efficient. Therefore, the EIS results demonstrate that higher Chl loadings lower the interfacial charge–transfer resistance, consistent with more efficient electron injection at the Chl-TNT interface. The divergence between photocurrent and R_{ct} trends can be attributed to enhanced carrier recombination and transport losses within thicker Chl films, which offset the benefit of reduced interfacial resistance.

To investigate exciton dynamics within the Chl layer, TRPL measurements were performed. In dilute acetone solution, Chl exhibited a fluorescence lifetime exceeding 3 ns (Figure 4a), indicative of spatially isolated chromophores with minimal nonradiative decay pathways [26, 27]. In contrast, when immobilized on TNT, the decay trace nearly coincides with the IRF (Figure 4a), showing that the excited-state population is quenched within the temporal resolution of the setup, consistent with ultrafast depopulation of Chl* via rapid electron injection into TiO_2. This reduction in exciton lifetime suggests the operation of rapid nonradiative decay routes, primarily arising from two mechanisms: (i) strong excitonic coupling within densely packed Chl domains, which facilitates energy delocalization [28, 29], and (ii) ultrafast electron injection from photoexcited Chl into the CB of TiO_2 [28, 30]. Together, these processes enable efficient exciton-to-charge conversion at the Chl-TNT interface.

At moderate Chl layer thicknesses (Figure 4c), exciton transport becomes more efficient through multi-step energy relay mechanisms involving both short-range hopping and longer-range dipole-mediated transfer. In this regime, closely packed Chl domains offer sufficient electronic coupling to support directional energy migration toward the TiO_2 interface [11, 31, 32]. This cooperative transport framework enables effective exciton harvesting and promotes interfacial charge injection, thereby enhancing photocurrent generation.

However, excessive Chl accumulation imposes both structural and photophysical limitations (Figure 4c). In highly dense pigment domains, strong interchromophoric interactions shorten exciton lifetimes to the sub-nanosecond scale and reduce exciton mobility within disordered regions. As a result, the effective diffusion length becomes confined to below 1 μm, restricting the spatial reach of exciton migration [6, 31]. Accordingly, at higher Chl loadings, corresponding to thicker films, the photocurrent output decreases (Figure 3a–c). This decline is attributed to increased structural disorder, trap-state formation, and nonradiative recombination, all of which hinder exciton transport and limit charge separation efficiency [6, 11].

At elevated Chl loadings, optical limitations begin to emerge. Transmittance measurements (Figure 4b) revealed that thicker Chl layers cause exponential attenuation of incident light, resulting in a depth-dependent reduction in photon flux. Consequently, photoexcitation becomes localized near the top surface of the photoelectrode, rendering the deeper regions effectively photoinactive. This spatial mismatch between the zones of light absorption and charge collection diminishes overall photocurrent, even in the presence of excess absorber materials. Therefore, optimal PEC performance is governed by a trade-off among light penetration depth, exciton diffusion length, and interfacial charge transfer efficiency.

Under the high light intensity (>100 mW cm^{-2}), an additional decline in photocurrent was observed despite the increased photon flux. This nonlinear response is attributed to photodegradation of the Chl layer, driven by the formation of reactive oxygen species (ROS) such as superoxide ($\cdot O_2^-$) and hydroxyl radicals (·OH). High irradiation enhances the generation of Chl* states, which in turn promotes ROS formation via energy or electron transfer to molecular oxygen and/or water (Supporting Information: Figure S11) [33]. These ROS subsequently degrade the Chl matrix, impairing both its light-harvesting capacity and interfacial charge–transfer functionality.

ijer, 2025, 1, Downloaded from https://onlinelibrary.wiley.com/doi/10.1155/er/3924822 by Chung-Ang University, Seoul, Wiley Online Library on [30/11/2025]. See the Terms and Conditions (https://onlinelibrary.wiley.com/terms-and-conditions) on Wiley Online Library for rules of use; OA articles are governed by the applicable Creative Commons License

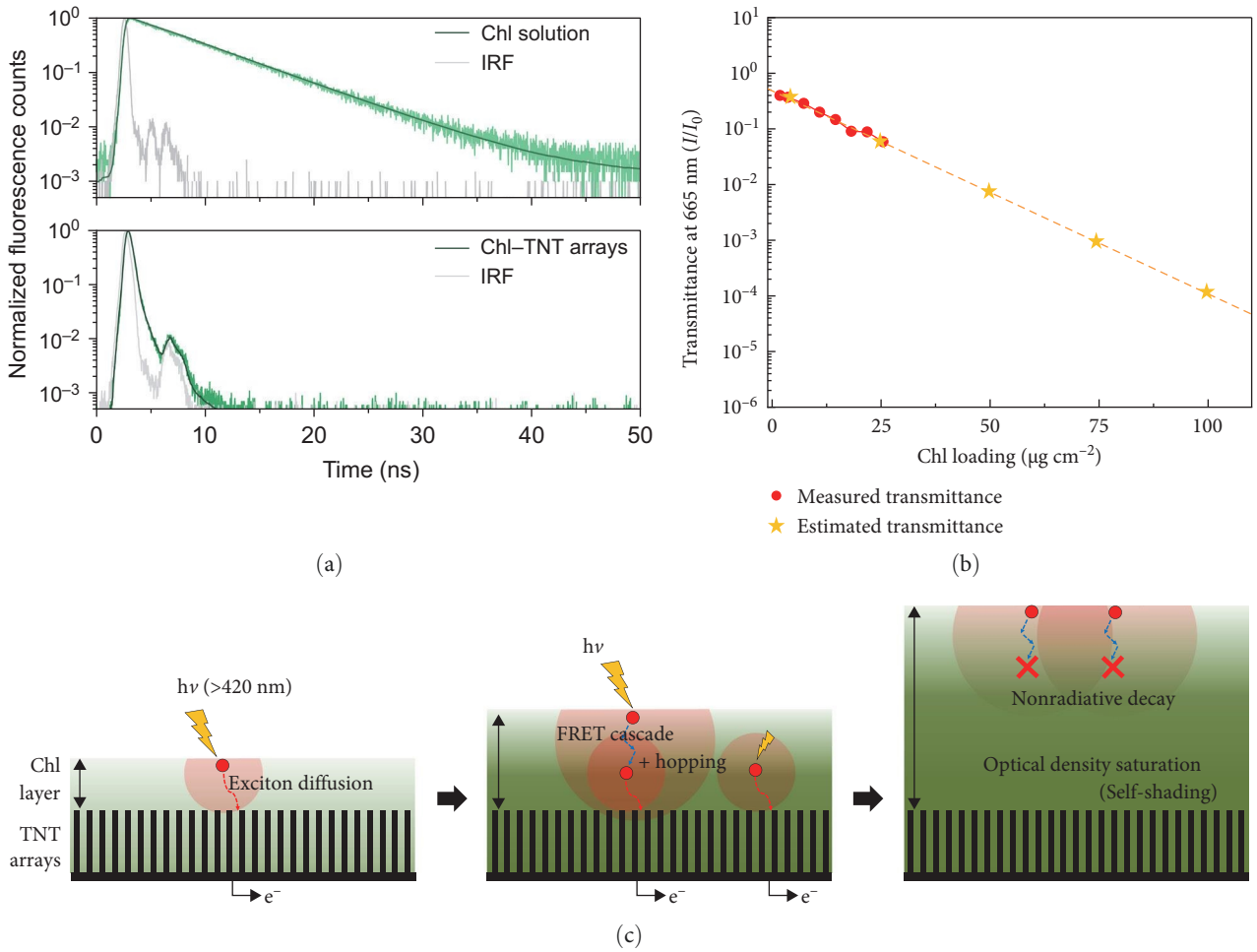


FIGURE 4: (a) Time-resolved photoluminescence decay profiles of Chl recorded at 660 nm emission following 405 nm excitation, comparing Chl in acetone solution and Chl immobilized on TiO_2 nanotube arrays. The instrument response function (IRF) shown for reference. (b) Transmittance of photoelectrodes at different areal Chl loadings. Red circles represent measured transmittance (at 665 nm) for Chl films on transparent substrates, while yellow stars denote estimated values for Chl-TiO_2 nanotube arrays at loadings of 25, 50, 75, and 100 μg cm^{-2}. (c) Schematic illustration of exciton transport regimes as a function of Chl layer thickness: exciton diffusion dominates at low thickness, while a combination of Förster-type cascade and hopping governs the intermediate regime; excessive thickness leads to non-radiative decay and optical self-shading.

4. Conclusion

This work moves the Chl-TNT platform from proof-of-concept to an engineerable module for visible-light PEC by establishing quantitative, mechanistic design rules. We show that performance peaks not with indiscriminate absorption but at a balance where exciton harvesting and interfacial electron injection are commensurate; nanoconfinement in ordered TNTs shortens transport paths and makes this balance tunable through Chl loading, photon flux, and tube geometry. Guided by this principle, a loading-flux map reveals a clear operating window, while TRPL links device response to instrument-limited quenching consistent with ultrafast charge transfer; fluorescence assays confirm negligible pigment loss (<0.05% over 15 h). Under optimum conditions, the electrode delivers $J_{sc} = 7.5\ \mu A\ cm^{-2}$ and $P_{max} = 1.76\ \mu W\ cm^{-2}$, an 8.4-fold improvement over pristine TNT, and outperforms previously reported Chl- or thylakoid-based TiO_2 photoelectrodes (Supporting Information: Table S3). In contrast, excessive loading or high flux induces roll-off through self-shading, exciton trapping, and ROS-driven degradation. Identifying this ROS-limited regime defines a practical stability boundary and a concrete target for improvement—via protective overlayers, antioxidant co-sensitizers, stronger anchoring chemistries, or more robust chlorins. Together, these results recast Chl-TNT as a predictive model system and chart a rational path toward durable, low-cost, and scalable biohybrid optoelectronic and catalytic electrodes.

Nomenclature

PEC: Photoelectrochemical
TNT: Titanium nanotube
Chl: Chlorophyll
IRF: Instrument response function
ROS: Reactive oxygen species
SOD: Superoxide dismutase

ijer, 2025, 1, Downloaded from https://onlinelibrary.wiley.com/doi/10.1155/er/3924822 by Chung-Ang University, Seoul, Wiley Online Library on [30/11/2025]. See the Terms and Conditions (https://onlinelibrary.wiley.com/terms-and-conditions) on Wiley Online Library for rules of use; OA articles are governed by the applicable Creative Commons License

TPRL: Time-resolved photoluminescence
FIB: Focused ion beam.

Data Availability Statement

The data that support the findings of this study are available from the corresponding author upon reasonable request.

Conflicts of Interest

The authors declare no conflicts of interest.

Funding

This work was supported by the National Research Foundation of Korea (NRF) grant funded by the Korea government (MSIT) (Grants RS–2023–00212255, RS-2023-00280278, and RS-2025-02214779), by the MSIT under the ITRC support program (Grant IITP-RS-2024-00436248) supervised by the IITP, by the Ministry of Education through the G-LAMP Program (Grant RS-2023-00285390), and the Basic Science Research Program (Grant RS-2021-NR060141). This research was also supported by the Regional Innovation System and Education (RISE) program through the Chungnam-RISE, funded by the Ministry of Education (MOE) and the Chungnam, Republic of Korea (Grant 2025-RISE-12-022).

Acknowledgments

Abraham Seo and Kanghyun Lee contributed equally to this work. The authors thank the Cooperative Equipment Center at KOREATECH.

Supporting Information

Additional supporting information can be found online in the Supporting Information section. (*Supporting Information*) Figures S1–S11 and Tables S1–S3 associated with this article can be found from the authors or the Wiley Online Library. These include the PEC setup and electrode configuration, the top- and cross-sectional SEM images of TNT arrays and Chl coatings, the dependence of PEC activity on tube diameter and film thickness, the Raman spectra of TNT arrays, the XRD patterns of pristine and Chl-TNT arrays, the XPS spectra of Ti 2p and O 1s regions, the Chl release study, the I-V characteristics of Chl-TNT photoelectrodes, the UV–vis diffuse reflectance spectra, and the ROS scavenger effects on photocurrent stability. In addition, Tables S1–S3 summarize the Chl areal loading, film thickness, effective density, deposited solution volume, peak photocurrent values, and a literature comparison of related chlorophyll- and thylakoid-based photoelectrodes. The Supporting Note provides the derivation and justification of chlorophyll quantification coefficients.

References

[1] X. Chen and S. S. Mao, "Titanium Dioxide Nanomaterials: Synthesis, Properties, Modifications and Applications," *Chemical Reviews* 107, no. 7 (2007): 2891–2959.

[2] F. E. Osterloh, "Inorganic Nanostructures for Photoelectrochemical and Photocatalytic Water Splitting," *Chemical Society Reviews* 42, no. 6 (2013): 2294–2320.

[3] H. Khan and M. U. H. Shah, "Modification Strategies of TiO_2-Based Photocatalysts for Enhanced Visible-Light Activity and Energy-Storage Ability: A Review," *Journal of Environmental Chemical Engineering* 11, no. 6 (2023): 111532.

[4] M. H. Sawal, A. A. Jalil, N. F. Khusnun, N. S. Hassan, and M. B. Bahari, "A Review of Recent Modification Strategies of TiO_2-Based Photoanodes for Efficient Photoelectrochemical Water-Splitting Performance," *Electrochimica Acta* 467 (2023): 143142.

[5] G. Buscemi, D. Vona, M. Trotta, F. Milano, and G. M. Farinola, "Chlorophylls as Molecular Semiconductors: Introduction and State of Art," *Advanced Materials Technologies* 7, no. 2 (2022): 2100245.

[6] H. van Amerongen, R. van Grondelle, and L. Valkunas, *Photosynthetic Excitons* (World Scientific, 2000).

[7] R. Irodia, M. Mîndroiu, I. Bîru, et al., "Double S-Scheme Polydopamine/TiO_2/Chlorophyll as Stable and Efficient Green Photoelectrocatalyst," *ChemElectroChem* 10, no. 24 (2023): e202300277.

[8] M. Onyemowo, Y. Unpaprom, and R. Ramaraj, "Exploring the Potential of Natural Dyes in DSSCs: Innovations for Efficient Light Harvesting and Charge Separation Through Co-Sensitization," *Optical Materials* 148 (2024): 114860.

[9] A. K. Arof and T. L. Ping, *Chlorophyll as Photosensitizer in Dye-Sensitized Solar Cells* (Chlorophyll, InTechOpen, 2017): 1–25.

[10] A. Kathiravan, M. Chandramohan, R. Renganathan, and S. Sekar, "Cyanobacterial Chlorophyll as a Sensitizer for Colloidal TiO_2," *Spectrochimica Acta Part A: Molecular and Biomolecular Spectroscopy* 71, no. 5 (2009): 1783–1787.

[11] R. E. Blankenship, *Molecular Mechanisms of Photosynthesis* (Wiley, 2002).

[12] L.-K. Tsui, J. Huang, M. Sabat, and G. Zangari, "Visible-Light Sensitization of TiO_2 Nanotubes by Bacteriochlorophyll-c Dyes for Photoelectrochemical Solar Cells," *ACS Sustainable Chemistry & Engineering* 2, no. 9 (2014): 2097–2101.

[13] L. Tian, Q. Xin, C. Zhao, et al., "Nanoarray Structures for Artificial Photosynthesis," *Small* 17, no. 38 (2021): 2006530.

[14] G. K. Mor, K. Shankar, M. Paulose, O. K. Varghese, and C. A. Grimes, "Use of Highly Ordered TiO_2 Nanotube Arrays in Dye-Sensitized Solar Cells," *Nano Letters* 6, no. 2 (2006): 215–218.

[15] H. N. Umh, S. Yu, Y. H. Kim, S. Y. Lee, and J. Yi, "Tuning the Structural Color of a 2D Photonic Crystal Using a Bowl-Like Nanostructure," *ACS Applied Materials & Interfaces* 8, no. 24 (2016): 15802–15808.

[16] A. M. Gilmore, V. P. Shinkarev, T. L. Hazlett, and Govindjee, "Quantitative Analysis of the Effects of Intrathylakoid pH and Xanthophyll-Cycle Pigments on Chlorophyll a Fluorescence Lifetime Distributions and Intensity in Thylakoids," *Biochemistry* 37, no. 39 (1998): 13582–13593.

[17] R. J. Porra, W. A. Thompson, and P. E. Kriedemann, "Determination of Accurate Extinction Coefficients and Simultaneous Equations for Assaying Chlorophylls a and b Extracted With Four Different Solvents," *Biochimica et Biophysica Acta (BBA) - Bioenergetics* 975, no. 3 (1989): 384–394.

[18] N. Yamauchi and A. E. Watada, "Regulated Chlorophyll Degradation in Spinach Leaves During Storage," *Journal of the American Society for Horticultural Science* 116, no. 1 (1991): 58–62.

ijer, 2025, 1, Downloaded from https://onlinelibrary.wiley.com/doi/10.1155/er/3924822 by Chung-Ang University, Seoul, Wiley Online Library on [30/11/2025]. See the Terms and Conditions (https://onlinelibrary.wiley.com/terms-and-conditions) on Wiley Online Library for rules of use; OA articles are governed by the applicable Creative Commons License

[19] O. K. Varghese and C. A. Grimes, "Appropriate Strategies for Determining the Photoconversion Efficiency of Water Photoelectrolysis Cells: A Review With Examples Using Titania Nanotube Array Photoanodes," *Solar Energy Materials and Solar Cells* 92, no. 4 (2008): 374–384.
[20] J. R. Martínez, A. Vázquez-Durán, G. Martínez-Castañón, G. Ortega-Zarzosa, S. A. Palomares-Sánchez, and F. Ruiz, "Coesite Formation at Ambient Pressure and Low Temperatures," *Advances in Materials Science and Engineering* 2008 (2008): 406067, 6.
[21] D. A. H. Hanaor and C. C. Sorrell, "Review of the Anatase to Rutile Phase Transformation," *Journal of Materials Science* 46, no. 4 (2011): 855–874.
[22] K. M. Kadish, K. M. Smith, and R. Guilard, *Handbook of Porphyrin Science* (World Scientific, 2022).
[23] S. Park, C. J. Steen, D. Lyska, et al., "Chlorophyll–carotenoid Excitation Energy Transfer and Charge Transfer in Nannochloropsis Oceanica for the Regulation of Photosynthesis," *Proceedings of the National Academy of Sciences* 116, no. 9 (2019): 3385–3390.
[24] S. Park, A. L. Fischer, C. J. Steen, et al., "Chlorophyll-Carotenoid Excitation Energy Transfer in High-Light-Exposed Thylakoid Membranes Investigated by Snapshot Transient Absorption Spectroscopy," *Journal of the American Chemical Society* 140, no. 38 (2018): 11965–11973.
[25] Y. Li, L. Lin, F. Wu, et al., "In Situ Modification of Bismuth Oxyhalide Photocatalysts With Natural Chlorophyll for Enhanced Photocatalytic Performance," *RSC Advances* 15, no. 7 (2025): 4820–4828.
[26] T. M. Nordlund and W. H. Knox, "Lifetime of Fluorescence From Light-Harvesting Chlorophyll a/b Proteins: Excitation-Intensity Dependence," *Biophysical Journal* 36, no. 1 (1981): 193–201.
[27] W. Wan, D. Hua, J. Le, T. He, Z. Yan, and C. Zhou, "Study of Laser-Induced Chlorophyll Fluorescence Lifetime Measurement and its Correction," *Measurement* 60 (2015): 64–70.
[28] D. I. G. Bennett, K. Amarnath, S. Park, C. J. Steen, J. M. Morris, and G. R. Fleming, "Models and Mechanisms of the Rapidly Reversible Regulation of Photosynthetic Light Harvesting," *Open Biology* 9, no. 4 (2019): 190043.
[29] S. Park, C. J. Steen, A. L. Fischer, and G. R. Fleming, "Snapshot Transient Absorption Spectroscopy: Toward In Vivo Investigations of Non-Photochemical Quenching Mechanisms," *Photosynthesis Research* 141, no. 3 (2019): 367–376.
[30] M. E. K. Fuziki, A. M. Tusset, O. A. A. dos Santos, and G. G. Lenzi, "Chlorophyll Sensitization of TiO_2: A Mini-Review," *Reactions* 4, no. 4 (2023): 766–778.
[31] L. Varvelo, J. K. Lynd, B. Citty, O. Kühn, and D. I. G. B. Raccah, "Formally Exact Simulations of Mesoscale Exciton Diffusion in a Light-Harvesting 2 Antenna Nanoarray," *The Journal of Physical Chemistry Letters* 14, no. 12 (2023): 3077–3083.
[32] W. Zhu, Y. Sun, J. Liu, et al., "Exciton Transport in Molecular-Semiconductor Crystals for a Spin-Optoelectronics Paradigm," *Chemistry – A European Journal* 27, no. 1 (2021): 222–227.
[33] J. Kim, J. Lee, S. Kim, et al., "Virucidal Activity of Cu-Doped TiO_2 Nanoparticles Under Visible-Light Illumination: Effect of Cu Oxidation State," *Journal of Hazardous Materials* 465 (2024): 133525.

ijer, 2025, 1, Downloaded from https://onlinelibrary.wiley.com/doi/10.1155/er/3924822 by Chung-Ang University, Seoul, Wiley Online Library on [30/11/2025]. See the Terms and Conditions (https://onlinelibrary.wiley.com/terms-and-conditions) on Wiley Online Library for rules of use; OA articles are governed by the applicable Creative Commons License